

# Lawrence Berkeley National Laboratory

## LBL Publications

### Title

High-Pressure Study of Perovskites and Postperovskites in the (Mg,Fe)GeO<sub>3</sub> System

### Permalink

<https://escholarship.org/uc/item/6194d8qk>

### Journal

Inorganic Chemistry, 56(14)

### ISSN

0020-1669

### Authors

Stan, Camelia V  
Dutta, Rajkrishna  
Cava, Robert J  
et al.

### Publication Date

2017-07-17

### DOI

10.1021/acs.inorgchem.7b00774

### Supplemental Material

<https://escholarship.org/uc/item/6194d8qk#supplemental>

Peer reviewed

# High-Pressure Study of Perovskites and Postperovskites in the (Mg,Fe)GeO<sub>3</sub> System

Camelia V. Stan,<sup>\*,†,‡,§</sup> Rajkrishna Dutta,<sup>§</sup> Robert J. Cava,<sup>†</sup> Vitali B. Prakapenka,<sup>⊥</sup> and Thomas S. Duffy<sup>§</sup>

<sup>†</sup>Department of Chemistry, Princeton University, Princeton, New Jersey 08544, United States

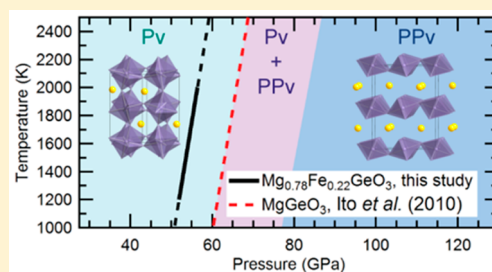
<sup>‡</sup>Advanced Light Source, Lawrence Berkeley National Laboratory, Berkeley, California 94720, United States

<sup>§</sup>Department of Geosciences, Princeton University, Princeton, New Jersey 08544, United States

<sup>⊥</sup>GeoSoilEnviroCARS, University of Chicago, Argonne National Lab, Argonne, Illinois 60439, United States

## Supporting Information

**ABSTRACT:** The effect of incorporation of Fe<sup>2+</sup> on the perovskite (*Pbnm*) and postperovskite (*Cmcm*) structures was investigated in the (Mg,Fe)GeO<sub>3</sub> system at high pressures and temperatures using laser-heated diamond anvil cell and synchrotron X-ray diffraction. Samples with compositions of Mg# ≥ 48 were shown to transform to the perovskite (~30 GPa and ~1500 K) and postperovskite (>55 GPa, ~1600–1800 K) structures. Compositions with Mg# ≥ 78 formed single-phase perovskite and postperovskite, whereas those with Mg# < 78 showed evidence for partial decomposition. The incorporation of Fe into the perovskite structure causes a decrease in octahedral distortion as well as a modest decrease in bulk modulus (*K*<sub>0</sub>) and a modest increase in zero-pressure volume (*V*<sub>0</sub>). It also leads to a decrease in the perovskite-to-postperovskite phase transition pressure by ~9.5 GPa over compositions from Mg#78 to Mg#100.



## INTRODUCTION

The discovery of the postperovskite (ppv) phase (CaIrO<sub>3</sub>-type, *Cmcm*) in MgSiO<sub>3</sub> at high pressure<sup>1</sup> has led to strong interest in perovskite (pv) to ppv phase transitions in other ABX<sub>3</sub> GdFeO<sub>3</sub>-type (*Pbnm*, X = O, F) pv in recent years. The ppv phase has been found in a variety of compositions, including Mg–Fe silicates, germanates (MnGeO<sub>3</sub><sup>2</sup> and MgGeO<sub>3</sub><sup>3</sup>), and a stannate (CaSnO<sub>3</sub><sup>4</sup>). A variety of transition-metal oxides of the form CaMO<sub>3</sub> (M = Ir, Rh, or Ru<sup>5,6</sup>) as well as several fluorides (NaMF<sub>3</sub>, M = Mg, Fe, Ni, Co, or Zn<sup>7–9</sup>) also undergoes this phase transition. Whereas GdFeO<sub>3</sub>-type pv consists of a network of corner-sharing BO<sub>6</sub> octahedra surrounding distorted eightfold coordinated A sites, ppv consists of corner- and edge-sharing BO<sub>6</sub> octahedral sheets alternating along the *b*-axis with face sharing anticubic eightfold coordinated A sites. The ability of a given pv to transform to the ppv structure has been found to be related to both the Goldschmidt tolerance factor  $t = (r_A/r_O)/\sqrt{2}(r_B/r_O)$  (where *r* is the ionic radius of A, B, or O) as well as to the degree of octahedral tilting relative to an ideal cubic pv [111] axis. This is primarily because the pv–ppv phase transition proceeds through a tilting/shear mechanism of the pv octahedral network accompanied by bond reconstruction.<sup>10</sup> Understating the effect of cation substitution on the properties of pv and ppv as well as on the pv–ppv phase transition is relevant to high-pressure geophysics, where it is believed that the anisotropic compressibility of ppv and the Clapeyron slope of the pv–ppv phase transition in (Mg,Fe)SiO<sub>3</sub> (the most abundant chemical species within the Earth's mantle) may be

responsible for a variety of seismic observations in the deep Earth.<sup>11</sup>

Germanates such as MgGeO<sub>3</sub> have long been used as analogues for silicates in studies of structure and phase transitions,<sup>12–16</sup> rheological<sup>17</sup> and magnetic properties,<sup>18–20</sup> and the behavior of glasses and melts.<sup>21–23</sup> Radius ratio considerations (Ge<sup>4+</sup> = 0.53 Å versus Si<sup>4+</sup> = 0.4 Å<sup>24</sup>) suggest that germanates will achieve higher-coordination environments at pressures lower than those of corresponding silicates: it has been found that the pv–ppv phase transition is lowered from 125 GPa in the case of MgSiO<sub>3</sub><sup>1</sup> to 63 GPa in the case of MgGeO<sub>3</sub>.<sup>25</sup> The Fe end members, FeGeO<sub>3</sub> and FeSiO<sub>3</sub>, have both been reported to decompose into oxides rather than form the pv phase at high pressures,<sup>15,26,27</sup> although other studies suggest FeGeO<sub>3</sub> pv may be stable.<sup>28–30</sup> To date, no high-pressure studies have been reported on intermediate compositions in the (Mg,Fe)GeO<sub>3</sub> system.

Here, we document an isomorphic model chemistry for silicates with similar phase transition pathways. Because the chemical leap from silicates to germanates is relatively small, this system is one of the closest analogue sets that can be used in this type of study. We report a synthesis of (Mg<sub>x</sub>Fe<sub>1–x</sub>)GeO<sub>3</sub> pyroxenes over a range of Mg/Fe compositions and investigate their high-pressure behavior using the laser-heated diamond anvil cell in conjunction with synchrotron X-ray diffraction.

Received: March 24, 2017

Published: June 26, 2017

## EXPERIMENTAL DETAILS

**Pyroxene Synthesis.** A suite of polycrystalline  $(\text{Mg}_x\text{Fe}_{1-x})\text{GeO}_3$  samples was prepared by solid-state ceramic sintering in evacuated silica tubes following the method of Redhammer et al.<sup>31</sup> For each composition,  $\text{GeO}_2$  (rutile-type),  $\text{MgO}$ ,  $\text{Fe}_2\text{O}_3$ , and  $\text{Fe}$  were ground under ethanol in stoichiometric proportions, dried, pelletized, and placed into silica tubes. The silica tubes were evacuated, welded shut, and heated to 1023 K for 3 days. After the initial heating, the samples were reground, placed into new silica tubes, and heated to 1223 K, a procedure that was repeated several times. Reaction completeness was evaluated between heating steps via powder X-ray diffraction. Characterization of the final synthesis products was carried out using high-resolution synchrotron powder X-ray diffraction at beamline 11-BM of the Advanced Photon Source (APS), Argonne National Laboratory. Chemical analysis of the samples was performed by electron microprobe and inductively coupled plasma mass spectrometry (ICP-MS) analysis. Major cation abundances (Mg, Fe, and Ge) were determined to  $\sim 0.5\%$  precision. The samples were also examined by Raman spectroscopy using a Horiba LabRam HR Evolution system.

**High-Pressure Experiments.** High-pressure experiments were carried out in symmetric-type diamond anvil cells (DACs) using anvils with 100–300  $\mu\text{m}$  diameter culets. Germanate samples were ground to a few micrometer grain size and mixed with 10 wt % gold powder (Goodfellow Corp., 99.95% purity), which served as a laser absorber and pressure calibrant. The mixtures were pressed into a thin layer and loaded into DACs using Ne as a quasi-hydrostatic pressure-transmitting medium. Diamond anvils were mounted on tungsten carbide or cubic boron nitride backing plates. Sample chambers were formed by drilling holes in Re gaskets that were preindented to 20–30  $\mu\text{m}$  thickness.

Angle-dispersive X-ray diffraction was performed at beamline 13-ID-D of the APS. X-rays with a wavelength of 0.3100 or 0.3344 Å were focused to a  $4 \times 3 \mu\text{m}$  beam size and directed through the diamond anvils, and the diffracted signal was collected with a Mar165 charge coupled device (CCD) detector. The detector position and orientation were calibrated using  $\text{LaB}_6$  as a standard. High temperatures were achieved by double-sided laser heating using two diode-pumped single-mode ytterbium fiber lasers ( $\lambda = 1064 \mu\text{m}$ ), each with output power up to 100 W. Beam-shaping optics were used to produce a flat-topped laser profile with a spot size of  $\sim 24 \mu\text{m}$ . Temperatures were measured from both sides of the sample by spectroradiometry. The laser power on each side of the sample was independently controlled to achieve uniformity of temperature across each sample to less than 50 K difference between upstream and downstream sides. Additional details of the X-ray diffraction and laser heating systems used here are reported elsewhere.<sup>32</sup>

X-ray diffraction patterns were typically collected for 30–120 s. In some cases, the cell was rotated by  $\pm 4^\circ$  in  $\omega$  during data collection to reduce preferred orientation effects. The two-dimensional CCD images were integrated to produce 1D diffraction patterns using the programs *DIOPTAS*<sup>33</sup> and *FIT2D*.<sup>34</sup> Initial peak positions were determined by fitting background-subtracted Voigt line shapes to the data. Pressure was determined from the (111) diffraction peak and thermal equation of state of gold.<sup>35</sup> Lattice parameters were refined by the LeBail method using *GSAS*<sup>36</sup> and *EXPGUI*.<sup>37</sup> For selected diffraction patterns, Rietveld refinements were also performed.

## RESULTS AND DISCUSSION

### Synthesis of Germanate Pyroxene Starting Materials.

The compositions of the  $(\text{Mg},\text{Fe})\text{GeO}_3$  pyroxenes were determined by ICP-MS and microprobe analysis to be Mg#100, Mg#92, Mg#78, Mg#61, and Mg#48, where  $\text{Mg\#} = \text{Mg}/(\text{Mg}+\text{Fe}) \times 100$  (see Table S1 in the Supporting Information). Microprobe analysis across several spots in selected samples showed little deviation, indicating that the elemental distribution was homogeneous. The measured compositions of the Mg#78 and Mg#48 samples yield an  $(\text{Mg}+\text{Fe})/\text{Ge}$  ratio lower than the expected pyroxene value,

suggesting the presence of excess  $\text{GeO}_2$ . Ambient-pressure X-ray diffraction patterns for all compositions are shown in Figure S1. All samples can be indexed as orthopyroxenes (space group *Pbc*). Lattice parameters for all compositions were determined via LeBail refinement of the synchrotron X-ray diffraction data (Table S2). The lattice parameters and volume of the  $\text{MgGeO}_3$  composition are similar to those previously reported.<sup>38,39</sup> The Mg#78 and Mg#48 samples were found to also contain minor rutile-type  $\text{GeO}_2$ , consistent with their slightly low  $(\text{Mg}+\text{Fe})/\text{Ge}$  ratios. The unit cell volumes and lattice parameters of  $(\text{Mg},\text{Fe})\text{GeO}_3$  orthopyroxene display a linear dependence on Mg# (Figure 1), as also observed in silicate orthopyroxenes.<sup>40</sup>

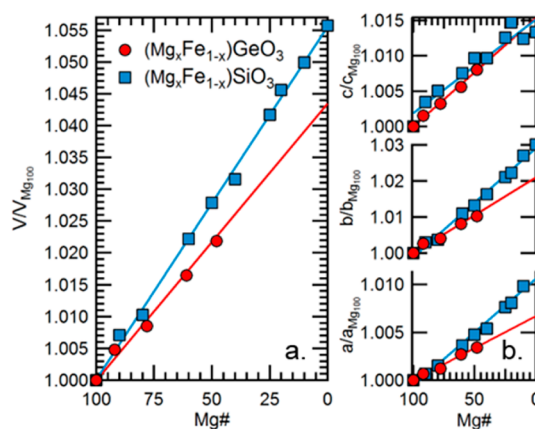


**Figure 1.** (a) Volume and (b) lattice parameters of silicate<sup>40</sup> and germanate orthopyroxenes as a function of Mg# at ambient conditions. Values are normalized to the magnesian end-member. Solid lines are linear fits to the data.

However, the germanates exhibit a relative dependence on the volume and *a*- and *b*-lattice parameters slightly smaller than those of the corresponding silicates.<sup>40</sup> This is expected, as the ionic radius of  $\text{Ge}^{4+}$  is larger than that of  $\text{Si}^{4+}$ , and so the volume and lattice parameter increase relative to the magnesian end-member will be smaller in germanates due to the larger overall volume of the germanate unit cell (900.0 and 830.4 Å<sup>3</sup>, respectively, for the Mg end-member). Raman spectra for all compositions are shown in Figure S2a. Raman frequencies of the Mg#100 sample match those reported by Ross and Navrotsky<sup>13</sup> (Table S3). The mode shifts of the major Raman peaks exhibit a linear frequency dependence on Mg# (Figure S2b), as observed in silicate orthopyroxenes.<sup>41</sup> Raman peaks broaden as a function of Fe content possibly due to cation disorder. These results indicate good chemical and structural homogeneity across the pyroxenes that are used as starting materials in the high-pressure experiments described below.

**Perovskite and Postperovskite Synthesis at High Pressures.** Upon room-temperature compression of the pyroxene samples in a diamond anvil cell to approximately 32 GPa, the observed diffraction peaks across all compositions became weak and broad and no longer corresponded with expected orthopyroxene positions. The samples were then laser heated. After less than 5 min of heating to 1500–1800 K, all compositions exhibited new diffraction peaks that could be attributed to the  $\text{GdFeO}_3$ -type (*Pbnm*) pv structure (Figure 2). The resulting lattice parameters for each composition are listed in Table 1, and a comparison of measured and calculated *d* spacings is given in Table S4. In the case of the Mg#61 and Mg#48 samples, peaks attributable to  $\text{GeO}_2$  as well as a few

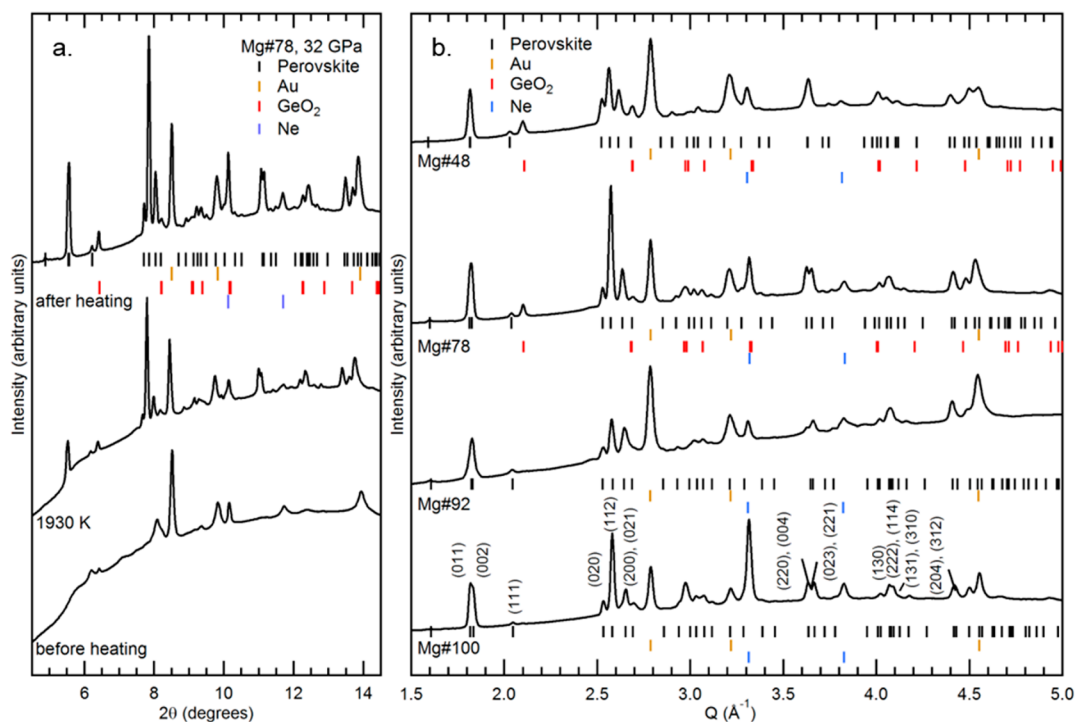


**Figure 2.** (a) Synthesis of Mg#78 perovskite at 32 GPa. (b) Representative X-ray diffraction patterns for (Mg,Fe)GeO<sub>3</sub> perovskites at room temperature after laser heating near 32 GPa (Table 2). Expected peak locations are shown by tick marks underneath each pattern. Selected Miller indices (*hkl*) are indicated.  $Q = 2\pi/d$  is used to compare data collected at different wavelengths.

**Table 1.** Perovskite and Postperovskite Unit Cell Parameters at Select Pressures

	<i>a</i> (Å)	<i>b</i> (Å)	<i>c</i> (Å)	<i>V</i> (Å <sup>3</sup> )	<i>P</i> (GPa)
			perovskite		
Mg#100	4.743(9)	4.966(9)	6.89(2)	162.4(5)	32.0
Mg#92	4.753(7)	4.970(8)	6.89(1)	162.9(4)	31.2
Mg#78	4.772(6)	4.974(7)	6.91(1)	164.0(3)	31.7
Mg#48	4.810(4)	4.981(4)	6.924(6)	165.9(2)	31.7
			postperovskite		
Mg#100	2.611(3)	8.450(9)	6.427(5)	141.8(2)	80.7
Mg#92	2.6938(4)	8.405(1)	6.3913(7)	139.34(5)	88.4
Mg#78	2.604(1)	8.442(3)	6.415(2)	141.0 (1)	85.3
Mg#61	2.621(6)	8.44(3)	6.421(8)	142.1(4)	78.6
Mg#48	2.621(2)	8.512(4)	6.458(4)	144.1(1)	76.3

peaks at high *d* spacing of unknown origin were also observed. For the Mg#48 sample, this may be due to excess GeO<sub>2</sub> observed in the starting material. The presence of GeO<sub>2</sub> peaks in the Mg#61 sample, however, may indicate a maximum solubility of iron in the pv structure, as has been observed for silicates.<sup>42</sup>

In a further set of experiments, previously unheated samples with composition between Mg#100–48 were first compressed to 70–80 GPa and then heated to ~1500–1900 K. Prior to heating, only weak broad peaks were observed in the starting material. Within 5 min of heating, those peaks disappeared, and peaks corresponding to the ppv phase appeared (Figure 3). For compositions with Mg# ≥ 78, all observed peaks could be indexed as ppv, Au, or Ne. At these pressures, GeO<sub>2</sub> is expected to be in the pyrite (*Pa* $\bar{3}$ ) phase, and its major diffraction peaks coincide with either ppv or Au; thus, its presence cannot be conclusively ruled out. For the Mg#61 and Mg#48 compositions, additional unexplained peaks were observed after prolonged heating, indicating possible decomposition or

chemical reaction. When ppv was synthesized for the Mg#48 composition at 103 GPa, no additional peaks were observed, suggesting that in compositions with higher Fe content (Mg# < 78), single-phase ppv can be synthesized at higher pressures.

Rietveld refinements were carried out on Mg#78 pv and ppv samples (Figure 4). The background was manually fit for each pattern using a Chebyshev polynomial and then refined. Once a good fit was found, Rietveld refinement was performed. First, phase fractions were allowed to refine. The atomic position of Fe was constrained to the same coordinates as those of Mg, and initial fractional coordinate estimates were made based on values reported for Mg#95 silicate pv<sup>43</sup> or Mg#100 germanate ppv.<sup>44</sup> Thermal displacement parameters were taken from Kubo et al.<sup>44</sup> and fixed throughout. The Mg:Fe ratio was also fixed based on microprobe results of the starting material. Fractional coordinates of all atoms were refined. Preferred orientation was accounted for in the case of pv, and sixth-order spherical harmonics in a cylindrical geometry were applied during the refinement. Final lattice parameters and atomic

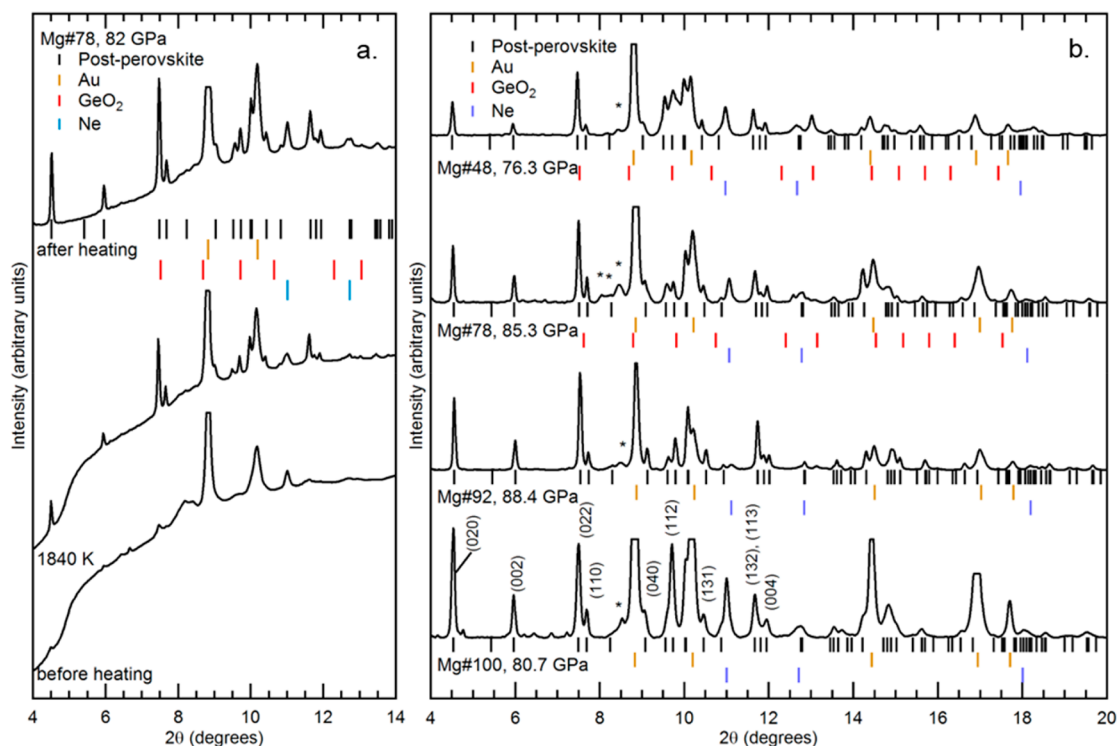


**Figure 3.** (a) Synthesis of Mg#78 postperovskite at 80.2 GPa. (b) Representative X-ray diffraction patterns for (Mg,Fe)GeO<sub>3</sub> postperovskites at room temperature after laser heating. Expected peak locations are shown below each pattern. Au peaks were truncated for clarity. Select Miller indices (*hkl*) are indicated. Asterisks denote diffuse peaks corresponding to single perovskite grains; these peaks disappear with annealing at higher pressures.

fractional coordinates for pv and ppv are listed in Table 2. We are not aware of any previous reports of Rietveld refinement on germanate pv compositions.

**Phase Relations.** The pv to ppv transition boundary was investigated for Mg#78 and Mg#100. Previously unheated samples were compressed at room temperature to pressures near the expected phase boundary, and then heated between 1000 and 2600 K in ~200 K intervals. Consistent with earlier studies,<sup>45–47</sup> we found that both pv and ppv could be synthesized rapidly from disordered starting material (especially at pressures well above or below the phase boundary), but once one phase formed, the transformation in both the forward and reverse direction was very sluggish unless significant over- or under-pressure was applied.

In Mg#100, the phase boundary is univariant, but we observe a wide pressure range over which both pv and ppv coexist due to the sluggish transition kinetics (Figure S3). The first appearance of ppv in this study corresponds well with the observations of Hirose et al.<sup>25</sup> and Ito et al.<sup>48</sup> Heating for 10–15 min intervals at a fixed pressure and temperature did not significantly alter the ratio of pv:ppv in the Mg#100 sample, in accordance with prior observations of slow reaction kinetics.<sup>48</sup> The presence of small amounts of pv in the sample even at high pressures suggests either the existence of a temperature gradient or that the transition from starting material to pv is kinetically more accessible despite the metastability of pv in this pressure and temperature regime. Coexistence of pv and ppv to high pressures was also observed by Hirose et al.<sup>25</sup> and Ito et al.<sup>48</sup>

In (Mg,Fe)SiO<sub>3</sub>, the pv to ppv phase transition is divariant with an expected coexistence region in pressure–temperature space. We observe the presence of both phases over a wide

range of 54–79 GPa and 1350–2575 K (Figure 5), but this may reflect kinetics as discussed above. Notably, the first appearance of ppv peaks occurs at pressure significantly lower than that in Mg#100 samples. This indicates that the presence of Fe lowers the pv to ppv phase transition pressure in germanates, similar to observations in silicates.<sup>46,49–52</sup> Our lower boundary for the pv–ppv two phase loop is indicated by a solid black line (Figure 5), assuming a Clapeyron slope similar to that of Ito et al.<sup>48</sup> We find that the inclusion of 22 at % Fe reduces the lower boundary of the divariant loop by ~9.5 GPa relative to Mg#100. We were unable to reliably determine the upper boundary of the two phase loop in Mg#78. However, we observe single phase ppv in Mg#78 at all pressures above 80 GPa and observed instances of single-phase Mg#78 ppv at pressure and temperature conditions as low as 1850 K and 70 GPa when synthesized from previously unheated material (Figure 5).

In an additional experiment, Mg#100 and Mg#78 samples were loaded adjacent to each other within the same cell, and pv was synthesized in each composition at 30 GPa by heating to 1600 K. These samples were then compressed to 74 GPa with heating to ~1700–1800 K every 5 GPa. At ~1700 K above 55.7 GPa, we observe evidence for the incipient formation of ppv in Mg#78 but not in Mg#100 (Figure S4). With increasing pressure, the intensity of the ppv peaks grows significantly in Mg#78. Ppv is not observed in Mg#100 below 74.0 GPa, at which point weak diffraction spots associated with this phase begin to appear. This supports our conclusion that the presence of Fe enhances ppv phase stability in germanates.

**Equations of State. Perovskite.** The equations of state of Mg#100 and Mg#78 pv were also measured using two adjacent samples in a separate loading. In this instance, pv was

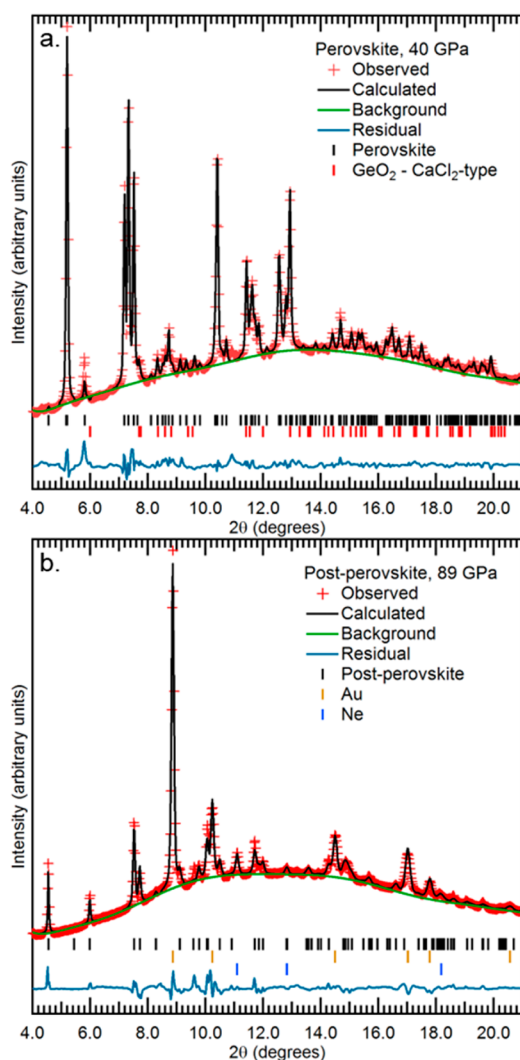


**Figure 4.** Rietveld refinement of Mg#78 (a) perovskite at 40 GPa ( $\chi^2 = 2.1$ ) and (b) postperovskite at 89 GPa ( $\chi^2 = 3.2$ ). Pressure was determined from the Raman edge of diamond<sup>39</sup> and the Au equation of state.<sup>35</sup>

synthesized at  $\sim 31$  GPa in each sample by laser heating to  $\sim 1900$  K with a laser spot size of  $24 \mu\text{m}$  at the full-width half-maximum (fwhm). The two samples were approximately  $34 \mu\text{m}$  apart, and X-ray diffraction patterns taken from the region between the two heating spots showed the presence of only unheated starting material. This indicates that no significant heating occurred between the two samples, and thus they

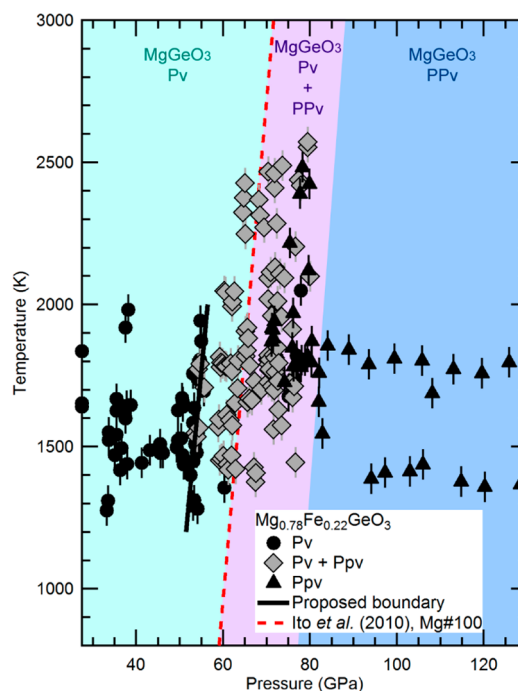


**Figure 5.** Mg#78 phases in pressure and temperature space. Color blocks indicate the Mg#100 perovskite–postperovskite observed phase distribution for comparison.

would not be expected to chemically interact. Pv samples were compressed up to 50 GPa in 2–3 GPa steps with laser annealing for 3–5 min at  $\sim 1500$  K every  $\sim 5$  GPa. Above 50 GPa, the samples were compressed in 2–3 GPa steps without further annealing to prevent conversion to the ppv phase. Unit cell volumes and lattice parameters as a function of pressure for Mg#78 and Mg#100 are plotted in Figure 6. To assess the possible degree of nonhydrostatic stress, we analyzed the fwhm of the Au(111) reflection as a function of pressure in both Mg#100 and Mg#78 (Figure S5). Up to 50 GPa, there is little change in the peak width. For Mg#100, the peak width increases above 50 GPa after annealing stopped, but no similar increase was observed for the Mg#78 sample.

Incorporation of Fe into the pv unit cell leads to an increase in the  $a$ -axis, a smaller increase in the  $c$  axis, and little change in the  $b$ -axis (Figure 6). This effect is similar to observations in silicate pv, where the  $a$ - and  $c$ -axes respond to Fe substitution more strongly than the  $b$ -axis, which appears to be almost insensitive to Fe content.<sup>46</sup> The effect of Fe incorporation can also be examined through its effect on the distortion of the pv

**Table 2.** Lattice Parameters and Atomic Positions from Rietveld Refinement of Mg#78 Perovskite and Postperovskite<sup>a</sup>

	perovskite –40 GPa				postperovskite –89.1 GPa			
	$a$ (Å)	$b$ (Å)	$c$ (Å)	$V$ (Å <sup>3</sup> )	$a$ (Å)	$b$ (Å)	$c$ (Å)	$V$ (Å <sup>3</sup> )
	4.7282(2)	4.9437(3)	6.8803(6)	160.83(1)	2.5980(8)	8.420(2)	6.399(2)	140.01(5)
	$x$	$y$	$z$	$F$	$x$	$y$	$z$	$F$
Mg	0.528(1)	0.5667(8)	0.25	0.78	0.0	0.251(2)	0.25	0.78
Fe	0.528(1)	0.5667(8)	0.25	0.22	0.0	0.251(2)	0.25	0.22
Ge	0.5	0.0	0.5	1	0.0	0.0	0.0	1
O1	0.126(3)	0.456(3)	0.25	1	0.0	0.937(4)	0.25	1
O2	0.185(2)	0.189(2)	0.559(2)	1	0.0	0.629(2)	0.442(4)	1
$\chi^2$	2.1				3.2			

<sup>a</sup>Atomic fraction ( $F$ ) was fixed to the value found by microprobe analysis.

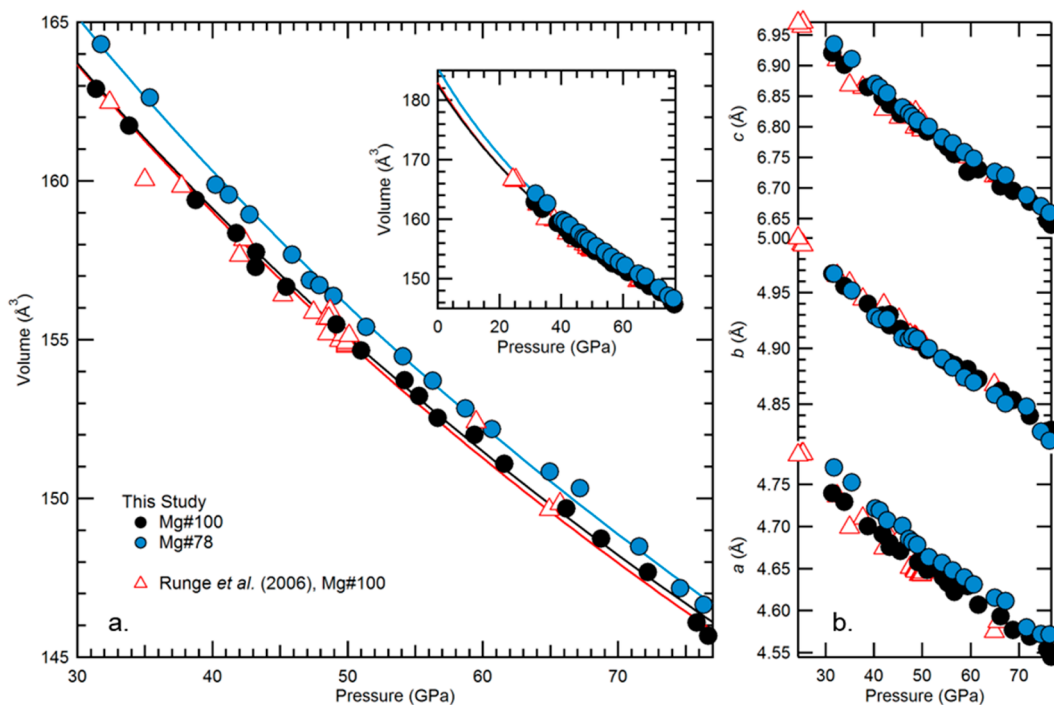


**Figure 6.** (a) Unit cell volumes and (b) lattice parameters of Mg#78 and Mg#100 perovskite measured upon compression. Lattice parameters were determined using LeBail refinement. Solid lines indicate Birch–Murnaghan equation of state fits with  $K_0'$  fixed at 4.

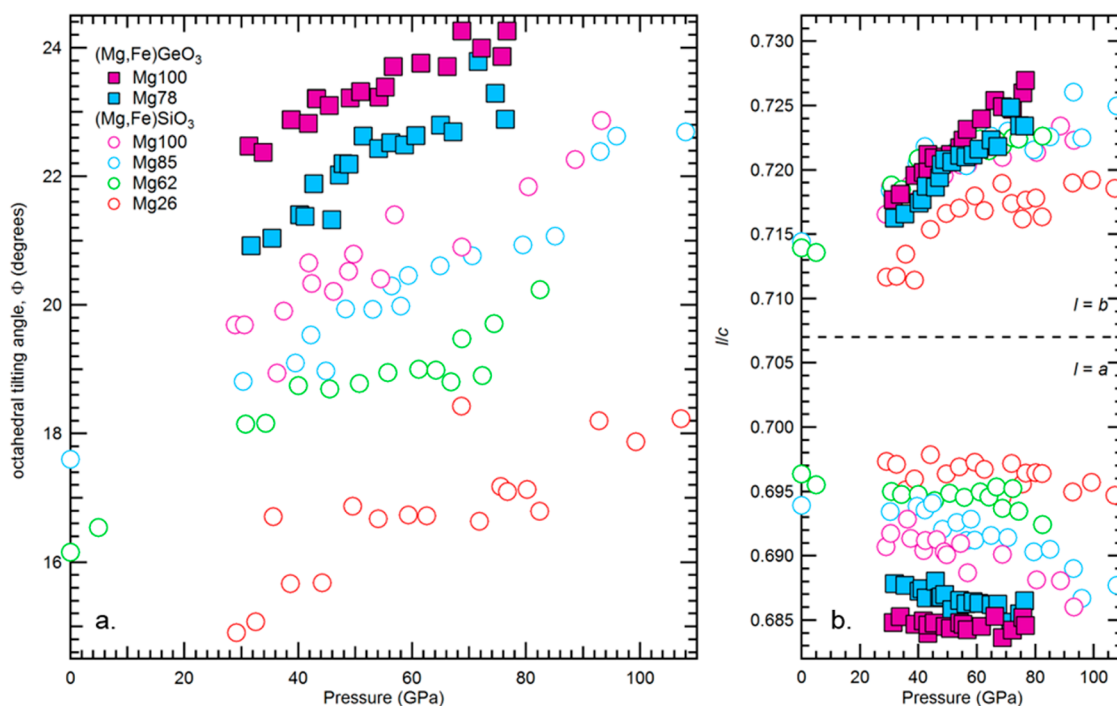


**Figure 7.** (a) Octahedral tilt,  $\Phi$ , and (b) lattice parameter ratios as a function of pressure in (Mg,Fe)GeO<sub>3</sub> and (Mg,Fe)SiO<sub>3</sub> perovskite. The dashed line in panel b corresponds to  $1/\sqrt{2}$ , the value expected for a cubic perovskite. (Mg,Fe)SiO<sub>3</sub> perovskite data is from Dorfman et al.<sup>46</sup>

away from ideal cubic symmetry. Assuming regular octahedra, the tilt,  $\Phi$ , i.e. of the octahedra about the cubic crystallographic  $\langle 111 \rangle$  axis, is defined as<sup>4,53,54</sup>

$$\Phi = \cos^{-1} \left( \frac{a^2 \sqrt{2}}{bc} \right)$$

In an ideal cubic pv,  $\Phi = 0$ . In both germanate and silicate pv,  $\Phi$  increases as a function of both pressure and Mg# (Figure 7a). This indicates that the structure becomes increasingly distorted with the application in pressure, but distortion decreases with incorporation of Fe.<sup>4</sup>

Lattice parameter ratios  $a/c$  and  $b/c$  are also used to characterize noncubic distortion in pv (Figure 7b). Both of these ratios are equal to  $1/\sqrt{2}$  (dashed line on Figure 7b) for a

cubic pv when described using an orthorhombic lattice. In both germanates and silicates,  $a/c$  increases with Fe content toward cubic values. There appears to be little dependence of  $a/c$  on pressure in silicate or germanate pv, although there is some evidence for an increase in distortion in silicates with high Fe contents above 80 GPa. Conversely, the  $b/c$  ratio shows less dependence on composition in both silicates and germanates but a stronger pressure effect with increasing pressure leading to greater deviation from the ideal value.

Overall, the  $a$ -lattice parameter shows the strongest dependence on Fe content in both silicate and germanate compositions, and all three parameters contribute to the pressure-induced distortion of the pv structure. The  $a$ - and  $c$ -axes exhibit similar compressibilities, while  $b$  is less compressible, producing the trends observed in Figure 7b. The addition of the larger  $\text{Fe}^{2+}$  cation into the A site of the pv thus leads to a reduction in the tilting of the octahedra surrounding the site. In effect,  $\text{Fe}^{2+}$  prevents the collapse of the octahedral cage around the A site, and  $\text{Fe}^{2+}$  incorporation causes the octahedral tilt to decrease primarily in the  $ac$ - and  $ab$ -planes. In contrast, the addition of pressure leads to an increase in octahedral tilt that is more pronounced along the  $bc$ - and  $ab$ -planes.

Unit cell volumes of the pv compositions were fit using the third order Birch–Murnaghan equation of state:

$$P(V) = \frac{3}{2}K_0 \left[ \left( \frac{V_0}{V} \right)^{7/3} - \left( \frac{V_0}{V} \right)^{5/3} \right] \left\{ 1 + \frac{3}{4}(K'_0 - 4) \left[ \left( \frac{V_0}{V} \right)^{2/3} - 1 \right] \right\}$$

where  $P$  is the pressure,  $K$  is the isothermal bulk modulus,  $K'$  is the pressure derivative of the bulk modulus,  $V$  is the unit cell volume, and the subscript 0 refers to ambient pressure conditions.  $K_0$  and  $V_0$  were fit by constraining  $K'_0$  to be either 4 or to the value of 3.7, as determined in previous study.<sup>55</sup> The results of the fits are presented in Table 3. Our results agree with an earlier study for Mg#100,<sup>55</sup> but the present data exhibit less scatter and cover a pressure range wider than that in the previous work (Figure 6). For a given  $K'_0$ , we observe a small decrease ( $\sim 7\%$ ) in  $K_0$  between Mg#100 and Mg#78, while the

fit value of  $V_0$  increases by 1.6%. In silicate pv, equation of state measurements indicate that  $V_0$  increases by 0.8% and that  $K_0$  does not change within uncertainty across a broad range of Mg–Fe substitution.<sup>46</sup> Overall, the germanate pv is more compressible than the corresponding silicates (e.g.,  $K_0 = 221$  GPa versus  $K_0 = 255$  GPa for Mg#100 germanate versus silicate pv) and has a higher  $V_0$  (e.g., 182.6 versus 162.3 Å<sup>3</sup> for Mg#100 germanate versus silicate pv).<sup>46,56</sup>

**Postperovskite.** The equation of state of Mg#100 ppv was measured in two separate runs. In the first run, starting material was compressed to  $\sim 75$ –80 GPa at room temperature and then converted to ppv by heating to  $\sim 1800$  K for 5 min. The sample was then compressed to 130 GPa in 2–5 GPa steps with annealing for 2–5 min at 1800 K every 5 GPa. In the second run, a pv sample at 76 GPa was heated to 1800 K for 12 min to induce phase transformation to ppv. Nevertheless, some weak pv peaks remained evident, and further heating was not performed. This sample was decompressed to 29 GPa, but no annealing was performed below 50 GPa to prevent conversion to pv. Differential stress was estimated from the measured lattice strain of Au using the method outlined by Singh et al.<sup>57,58</sup> Our results indicate that differential stresses in Au were between 0.5 and 1.3 GPa, consistent with those reported in prior equation of state studies of this composition.<sup>3</sup>

Third-order Birch–Murnaghan equation of state fits of the unit cell volumes as a function of pressure are reported in Table 3.  $K'_0$  was fixed in these fits to 4 or 4.4, which are the values previously used in studies of silicate ppv.<sup>3</sup> The volume and lattice parameter measurements as well as the calculated  $K_0$  and  $V_0$  of Mg#100 match prior studies,<sup>3,44</sup> but the current work exhibits less scatter (Figure 8). A comparison of equation of state fits shows that the Mg#100 ppv  $V_0$  is 3.7% smaller than that of pv, while  $K_0$  is 9% larger. The ppv lattice parameter ratios measured here also exhibit behavior similar to that found by Kubo et al.<sup>3,44</sup> (Figure S6) with  $b/a$  showing a response to pressure greater than that of  $c/a$ . This effect is more pronounced in germanates than in silicates and is due to greater compressibility along the  $b$ -axis (the direction of layer stacking in the ppv structure). This may suggest that the germanate octahedra display increased compressibility relative to that of their silicate counterparts.

## CONCLUSIONS

Orthopyroxene germanates were synthesized in the  $(\text{Mg}_x\text{Fe}_{1-x})\text{GeO}_3$  system with compositions between  $x = 100$ –48. The samples show a linear dependence of unit cell volume and Raman shift on Fe content. High-pressure experiments were carried out in the laser-heated diamond anvil cell coupled with synchrotron X-ray diffraction. Single-phase perovskite and postperovskite were obtained for compositions with Mg#  $\geq 78$  at 30 GPa and 1500–1800 K and 70 GPa and 1500–1900 K, respectively. Evidence for possible decomposition was observed in Mg#61 and Mg#48, indicating that these compositions may not be able to fully incorporate large amounts of Fe in their structures. Fe substitution into the perovskite A site leads to a decrease in distortion of perovskite relative to the cubic ideal, similar to observations in silicates. This is manifested mainly through an increase in the  $a$ -lattice parameter of the perovskite unit cell relative to  $b$  and  $c$ . We find that Fe substitution may lead to a slight decrease in the bulk modulus as a function of Fe content in perovskite. The equations of state of Mg#100 and Mg#78 pv and Mg#100 postperovskite were determined. The Mg#100

**Table 3. (Mg,Fe)GeO<sub>3</sub> Equation of State Parameters in Perovskite and Postperovskite from Experimental Studies**

	$V_0$ (Å <sup>3</sup> )	$K_0$ (GPa)	$K'_0$
	perovskite		
this study, Mg#100	182.6(5)	221(4)	4 <sup>b</sup>
	181.7(4)	236(4)	3.7 <sup>b</sup>
this study, Mg#78	185.5(3)	205(3)	4 <sup>b</sup>
	184.6(3)	219(3)	3.7 <sup>b</sup>
Runge et al., <sup>55</sup> Mg#100	182.9(3)	216(3)	4 <sup>b</sup>
	182.2(3)	229(3)	3.7 <sup>b</sup>
	180.16(5)	221.3(7)	3.90 <sup>a</sup>
	postperovskite		
this study, Mg#100	175.9(3)	241(3)	4 <sup>b</sup>
	177.5(3)	216(3)	4.4 <sup>b</sup>
Kubo et al., <sup>3</sup> Mg#100	175.9(5)	245(5)	4 <sup>b</sup>
	179.2(7)	207(5)	4.4 <sup>b</sup>
	178.0	201.9	4.3 <sup>a</sup>
Hirose et al., <sup>25</sup> Mg#100	183.1 ± 0.8	192 ± 5	4 <sup>b</sup>

<sup>a</sup>Theoretical calculation. <sup>b</sup>Value fixed during fit.

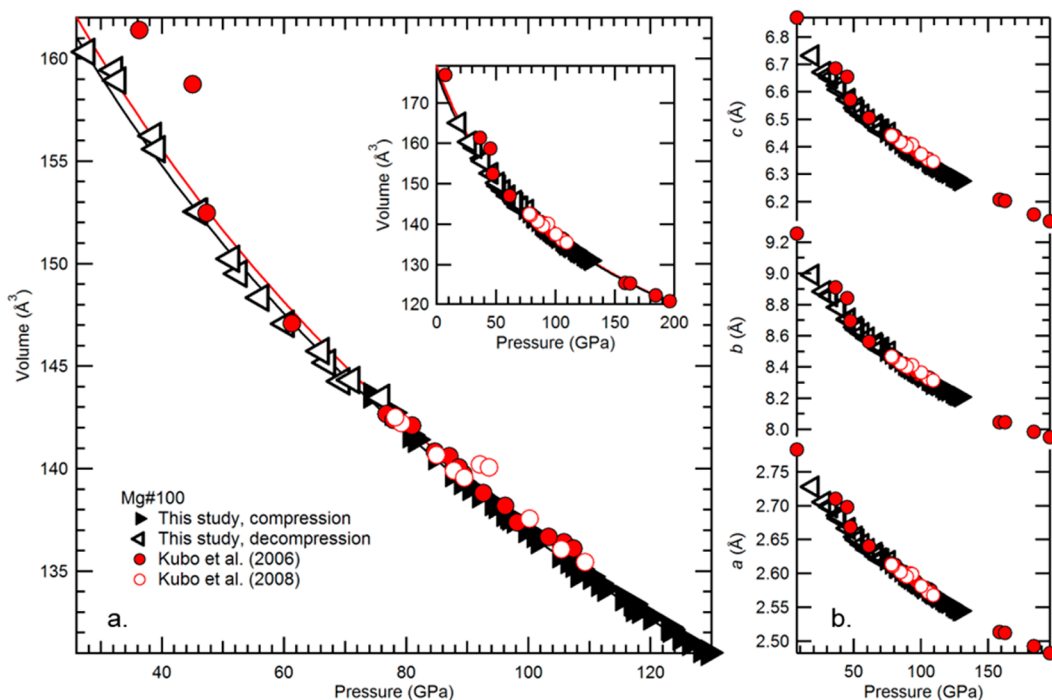


**Figure 8.** (a) Unit cell volume and (b) lattice parameters of  $\text{MgGeO}_3$  postperovskite upon both compression and decompression. Lines indicate Birch–Murnaghan equation of state fits with  $K_0'$  fixed at 4.

postperovskite equation of state is in good agreement with that in prior studies.<sup>3</sup> We also find that Fe substitution lowers the perovskite–postperovskite phase transition boundary, up to  $\sim 9.5$  GPa in the case of the Mg#78 composition. Overall, our results confirm that germanate perovskite and postperovskite with  $\text{Mg}\# \geq 78$  function as good analogues for the corresponding silicates with regard to structural and phase transition behavior.

## ■ ASSOCIATED CONTENT

### Supporting Information

The Supporting Information is available free of charge on the ACS Publications website at DOI: 10.1021/acs.inorgchem.7b00774.

Details of experimental results for both X-ray diffraction and Raman experiments at low and high pressure (PDF)

## ■ AUTHOR INFORMATION

### Corresponding Author

\*E-mail: cstan@lbl.gov.

### ORCID

Camelia V. Stan: 0000-0002-5025-5568

### Notes

The authors declare no competing financial interest.

## ■ ACKNOWLEDGMENTS

Drs. G. Finkelstein, J. Wicks, J. Krizan, J. Armstrong, and K. Crispin and the staff at APS beamlines 11-BM and 13-ID provided experimental assistance. This work was supported by the National Science Foundation (NSF) Grant EAR-1415321. Synthetic work was supported by the United States (US) Department of Energy (DOE), Division of Basic Energy Sciences, Grant DE-FG02-08ER46544. We acknowledge the use of GeoSoilEnviroCARS, which is supported by the NSF

(Grant EAR-1634415), and the DOE (Grant DE-FG02-94ER14466). The use of the high-pressure gas loading system was supported by GeoSoilEnviroCARS, and the Consortium for Materials Properties Research in the Earth Sciences, under NSF Cooperative Agreement EAR-1606856. Use of the Advanced Photon Source, operated for the DOE by Argonne National Laboratory, was supported by the DOE under Contract DE-AC02-06CH11357. This research used resources of the Advanced Light Source, which is a DOE Office of Science User Facility under Contract DE-AC02-05CH11231.

## ■ REFERENCES

- (1) Murakami, M.; Hirose, K.; Kawamura, K.; Sata, N.; Ohishi, Y. Post-Perovskite Phase Transition in  $\text{MgSiO}_3$ . *Science* **2004**, *304*, 855–858.
- (2) Tateno, S.; Hirose, K.; Sata, N.; Ohishi, Y. High-Pressure Behavior of  $\text{MnGeO}_3$  and  $\text{CdGeO}_3$  Perovskites and the Post-Perovskite Phase Transition. *Phys. Chem. Miner.* **2006**, *32*, 721–725.
- (3) Kubo, A.; Kiefer, B.; Shen, G.; Prakapenka, V. B.; Cava, R. J.; Duffy, T. S. Stability and Equation of State of the Post-Perovskite Phase in  $\text{MgGeO}_3$  to 2 Mbar. *Geophys. Res. Lett.* **2006**, *33*, L12S12.
- (4) Tateno, S.; Hirose, K.; Sata, N.; Ohishi, Y. Structural Distortion of  $\text{CaSnO}_3$  Perovskite under Pressure and the Quenchable Post-Perovskite Phase as a Low-Pressure Analogue to  $\text{MgSiO}_3$ . *Phys. Earth Planet. Inter.* **2010**, *181*, 54–59.
- (5) Akaogi, M.; Shirako, Y.; Kojitani, H.; Takamori, S.; Yamaura, K.; Takayama-Muromachi, E. Post-Perovskite Transitions in  $\text{CaB}^{++}\text{O}_3$  at High Pressure. *J. Phys. Conf. Ser.* **2010**, *215*, 012095.
- (6) Kojitani, H.; Shirako, Y.; Akaogi, M. Post-Perovskite Phase Transition in  $\text{CaRuO}_3$ . *Phys. Earth Planet. Inter.* **2007**, *165*, 127–134.
- (7) Yusa, H.; Shirako, Y.; Akaogi, M.; Kojitani, H.; Hirao, N.; Ohishi, Y.; Kikegawa, T. Perovskite-to-Postperovskite Transitions in  $\text{NaNiF}_3$  and  $\text{NaCoF}_3$  and Disproportionation of  $\text{NaCoF}_3$  Postperovskite under High Pressure and High Temperature. *Inorg. Chem.* **2012**, *51*, 6559–6566.
- (8) Martin, C. D.; Crichton, W. A.; Liu, H.; Prakapenka, V.; Chen, J.; Parise, J. B. Rietveld Structure Refinement of Perovskite and Post-

Perovskite Phases of NaMgF<sub>3</sub> (Neighborite) at High Pressures. *Am. Mineral.* **2006**, *91*, 1703–1706.

(9) Yakovlev, S.; Avdeev, M.; Mezouar, M. High-Pressure Structural Behavior and Equation of State of NaZnF<sub>3</sub>. *J. Solid State Chem.* **2009**, *182*, 1545–1549.

(10) Xiao, P.; Cheng, J.-G.; Zhou, J.-S.; Goodenough, J. B.; Henkelman, G. Mechanism of the CaIrO<sub>3</sub> Post-Perovskite Phase Transition under Pressure. *Phys. Rev. B: Condens. Matter Mater. Phys.* **2013**, *88*, 1 DOI: 10.1103/PhysRevB.88.144102.

(11) Shim, S. H. The Postperovskite Transition. *Annu. Rev. Earth Planet. Sci.* **2008**, *36*, 569.

(12) Navrotsky, A.; Hughes, L., Jr. Thermodynamic Relations among Olivine, Spinel, and Phenacite Structures in Silicates and Germanates. V. The System MgO-FeO-GeO<sub>2</sub>. *J. Solid State Chem.* **1976**, *16*, 185.

(13) Ross, N. L.; Navrotsky, A. Study of the MgGeO<sub>3</sub> Polymorphs (Orthopyroxene, Clinopyroxene, and Ilmenite Structures) by Calorimetry, Spectroscopy, and Phase Equilibria. *Am. Mineral.* **1988**, *73*, 1355–1365.

(14) Ringwood, A. E. The Constitution of the mantle—I: Thermodynamics of the Olivine-Spinel Transition. *Geochim. Cosmochim. Acta* **1958**, *13*, 303–321.

(15) Ringwood, A. E.; Seabrook, M. High-Pressure Phase Transformation in Germanate Pyroxenes and Related Compounds. *J. Geophys. Res.* **1963**, *68*, 4601.

(16) Akaogi, M.; Kojitani, H.; Yusa, H.; Yamamoto, R.; Kido, M.; Koyama, K. High-Pressure Transitions and Thermochemistry of MgGeO<sub>3</sub> (M = Mg, Zn and Sr) and Sr-Silicates: Systematics in Enthalpies of Formation of A<sup>2+</sup>B<sup>4+</sup>O<sub>3</sub> Perovskites. *Phys. Chem. Miner.* **2005**, *32*, 603–613.

(17) Merkel, S.; Kubo, A.; Miyagi, L.; Speziale, S.; Duffy, T. S.; Mao, H.-K.; Wenk, H.-R. Plastic Deformation of MgGeO<sub>3</sub> Post-Perovskite at Lower Mantle Pressures. *Science* **2006**, *311*, 644–646.

(18) Lambruschi, E.; Aliatis, I.; Mantovani, L.; Tribaudino, M.; Bersani, D.; Redhammer, G. J.; Lottici, P. P. Raman Spectroscopy of CaM<sup>2+</sup>Ge<sub>2</sub>O<sub>6</sub> (M<sup>2+</sup> = Mg, Mn, Fe, Co, Ni, Zn) Clinopyroxenes. *J. Raman Spectrosc.* **2015**, *46*, 586–590.

(19) Nestola, F.; Redhammer, G. J.; Pamato, M. G.; Secco, L.; Dal Negro, A. High-Pressure Phase Transformation in LiFeGe<sub>2</sub>O<sub>6</sub> Pyroxene. *Am. Mineral.* **2009**, *94*, 616–621.

(20) Novikov, G. V.; Sipavina, L. V.; Hafner, S. S. Low Temperature Magnetic Transitions in Chain Germanates. *Solid State Commun.* **1995**, *95*, 405–408.

(21) Ohtaka, O.; Arima, H.; Fukui, H.; Utsumi, W.; Katayama, Y.; Yoshiasa, A. Pressure-Induced Sharp Coordination Change in Liquid Germanate. *Phys. Rev. Lett.* **2004**, *92*, 155506.

(22) Vaccari, M.; Aquilanti, G.; Pascarelli, S.; Mathon, O. A New EXAFS Investigation of Local Structural Changes in Amorphous and Crystalline GeO<sub>2</sub> at High Pressure. *J. Phys.: Condens. Matter* **2009**, *21*, 145403.

(23) Henderson, G. S.; Wang, H. M. Germanium Coordination and the Germanate Anomaly. *Eur. J. Mineral.* **2002**, *14*, 733–744.

(24) Shannon, R. D. Revised Effective Ionic Radii and Systematic Studies of Interatomic Distances in Halides and Chalcogenides. *Acta Crystallogr., Sect. A: Cryst. Phys., Diffr., Theor. Gen. Crystallogr.* **1976**, *32*, 751–767.

(25) Hirose, K.; Kawamura, K.; Ohishi, Y.; Tateno, S.; Sata, N. Stability and Equation of State of MgGeO<sub>3</sub> Post-Perovskite Phase. *Am. Mineral.* **2005**, *90*, 262–265.

(26) Liu, L. The Post-Spinel Phases of Twelve Silicates and Germanates. In *High-Pressure Research: Application to Geophysics*; Manghnani, M. H., Akimoto, S.-I., Eds.; Academic Press: New York, NY, 1977; pp 245–253.

(27) Ming, L. C.; Bassett, W. A. Decomposition of FeSiO<sub>3</sub> into FeO + SiO<sub>2</sub> under Very High Pressure and High Temperature. *Earth Planet. Sci. Lett.* **1975**, *25*, 68–70.

(28) Nagai, T.; Hattori, T.; Tsuchiya, T.; Yamanaka, T. First Observation of FeGeO<sub>3</sub>-Perovskite under High Pressure. *Solid State Commun.* **1998**, *107*, 223–225.

(29) Hattori, T.; Matsuda, T.; Tsuchiya, T.; Nagai, T.; Yamanaka, T. Clinopyroxene-Perovskite Phase Transition of FeGeO<sub>3</sub> under High Pressure and Room Temperature. *Phys. Chem. Miner.* **1999**, *26*, 212–216.

(30) Yamanaka, T.; Mao, W. L.; Ganesh, P.; Shulenburg, L.; Mao, H.; Hemley, R. J. High-Pressure Polymorphs of Iron-Rich (Mg,Fe)-SiO<sub>3</sub> and FeGeO<sub>3</sub> Perovskite and Post-Perovskite, Abstract MR32A-01 presented at 2010 Fall Meeting, AGU, San Francisco, CA, December 13–17, 2010.

(31) Redhammer, G. J.; Senyshyn, A.; Tippelt, G.; Pietzonka, C.; Treutmann, W.; Roth, G.; Amthauer, G. Magnetic and Low-Temperature Structural Behavior of Clinopyroxene-Type FeGeO<sub>3</sub>: A Neutron Diffraction, Magnetic Susceptibility, and <sup>57</sup>Fe Mössbauer Study. *Am. Mineral.* **2012**, *97*, 694.

(32) Prakapenka, V. B.; Kubo, A.; Kuznetsov, A.; Laskin, A.; Shkurikhin, O.; Dera, P.; Rivers, M. L.; Sutton, S. R. Advanced Flat Top Laser Heating System for High Pressure Research at GSECARS: Application to the Melting Behavior of Germanium. *High Pressure Res.* **2008**, *28*, 225–235.

(33) Prescher, C.; Prakapenka, V. B. DIOPTAS: A Program for Reduction of Two-Dimensional X-Ray Diffraction Data and Data Exploration. *High Pressure Res.* **2015**, *35*, 223–230.

(34) Hammersley, A. P.; Svensson, S. O.; Hanfland, M.; Fitch, A. N.; Häussermann, D. Two-Dimensional Detector Software: From Real Detector to Idealized Image or Two-Theta Scan. *High Pressure Res.* **1996**, *14*, 235–248.

(35) Fei, Y.; Ricolleau, A.; Frank, M.; Mibe, K.; Shen, G.; Prakapenka, V. Toward an Internally Consistent Pressure Scale. *Proc. Natl. Acad. Sci. U. S. A.* **2007**, *104*, 9182–9186.

(36) Larson, A. C.; Von Dreele, R. B. General Structure Analysis System (GSAS). *Los Alamos National Laboratory Report LAUR* **2000**, 86–748.

(37) Toby, B. H. EXPGUI, a Graphical User Interface for GSAS. *J. Appl. Crystallogr.* **2001**, *34*, 210–213.

(38) Ozima, M. Structure of Orthopyroxene-Type and Clinopyroxene-Type Magnesium Germanium Oxide MgGeO<sub>3</sub>. *Acta Crystallogr., Sect. C: Cryst. Struct. Commun.* **1983**, *39*, 1169–1172.

(39) Robbins, C. R.; Levin, E. M. The System Magnesium Oxide-Germanium Dioxide. *Am. J. Sci.* **1959**, *257*, 63–70.

(40) Turnock, A. C.; Lindsley, D. H.; Grover, J. E. Synthesis and Unit Cell Parameters of Ca-Mg-Fe Pyroxenes. *Am. Mineral.* **1973**, *58*, 50–59.

(41) Stalder, R.; Kronz, A.; Schmidt, B. C. Raman Spectroscopy of Synthetic (Mg,Fe)SiO<sub>3</sub> Single Crystals. An Analytical Tool for Natural Orthopyroxenes. *Eur. J. Mineral.* **2009**, *21*, 27–32.

(42) Mao, H.; Shen, G.; Hemley, R. J. Multivariable Dependence of Fe-Mg Partitioning in the Lower Mantle. *Science* **1997**, *278*, 2098–2100.

(43) Jephcoat, A. P.; Hriljac, J. A.; McCammon, C. A.; O'Neill, H. S. C.; Rubie, D. C.; Finger, L. W. High-Resolution Synchrotron X-Ray Powder Diffraction and Rietveld Structure Refinement of Two (Mg<sub>0.95</sub>Fe<sub>0.05</sub>)SiO<sub>3</sub> Perovskite Samples Synthesized under Different Oxygen Fugacity Conditions. *Am. Mineral.* **1999**, *84*, 214–220.

(44) Kubo, A.; Kiefer, B.; Shim, S.-H.; Shen, G.; Prakapenka, V. B.; Duffy, T. S. Rietveld Structure Refinement of MgGeO<sub>3</sub> Post-Perovskite Phase to 1 Mbar. *Am. Mineral.* **2008**, *93*, 965–976.

(45) Shieh, S. R.; Dorfman, S. M.; Kubo, A.; Prakapenka, V. B.; Duffy, T. S. Synthesis and Equation of State of Post-Perovskites in the (Mg,Fe)<sub>3</sub>Al<sub>2</sub>Si<sub>3</sub>O<sub>12</sub> System. *Earth Planet. Sci. Lett.* **2011**, *312*, 422–428.

(46) Dorfman, S. M.; Meng, Y.; Prakapenka, V. B.; Duffy, T. S. Effects of Fe-Enrichment on the Equation of State and Stability of (Mg,Fe)SiO<sub>3</sub> Perovskite. *Earth Planet. Sci. Lett.* **2013**, *361*, 249–257.

(47) Dorfman, S. M.; Shieh, S. R.; Meng, Y.; Prakapenka, V. B.; Duffy, T. S. Synthesis and Equation of State of Perovskites in the (Mg,Fe)<sub>3</sub>Al<sub>2</sub>Si<sub>3</sub>O<sub>12</sub> System to 177 GPa. *Earth Planet. Sci. Lett.* **2012**, *357–358*, 194–202.

(48) Ito, E.; Yamazaki, D.; Yoshino, T.; Fukui, H.; Zhai, S.; Shatzkiy, A.; Katsura, T.; Tange, Y.; Funakoshi, K. Pressure Generation and Investigation of the Post-Perovskite Transformation in MgGeO<sub>3</sub> by

Squeezing the Kawai-Cell Equipped with Sintered Diamond Anvils. *Earth Planet. Sci. Lett.* **2010**, *293*, 84–89.

(49) Mao, W. L.; Shen, G.; Prakapenka, V. B.; Meng, Y.; Campbell, A. J.; Heinz, D. L.; Shu, J.; Hemley, R. J.; Mao, H.-K. Ferromagnesian Postperovskite Silicates in the D'' Layer of the Earth. *Proc. Natl. Acad. Sci. U. S. A.* **2004**, *101*, 15867–15869.

(50) Shieh, S. R.; Duffy, T. S.; Kubo, A.; Shen, G.; Prakapenka, V. B.; Sata, N.; Hirose, K.; Ohishi, Y. Equation of State of the Postperovskite Phase Synthesized from a Natural (Mg,Fe)SiO<sub>3</sub> Orthopyroxene. *Proc. Natl. Acad. Sci. U. S. A.* **2006**, *103*, 3039–3043.

(51) Caracas, R.; Cohen, R. E. Effect of Chemistry on the Stability and Elasticity of the Perovskite and Post-Perovskite Phases in the MgSiO<sub>3</sub>-FeSiO<sub>3</sub>-Al<sub>2</sub>O<sub>3</sub> System and Implications for the Lowermost Mantle. *Geophys. Res. Lett.* **2005**, *32*, L16310.

(52) Stackhouse, S.; Brodholt, J. P.; Price, G. D. Elastic Anisotropy of FeSiO<sub>3</sub> End-Members of the Perovskite and Post-Perovskite Phases. *Geophys. Res. Lett.* **2006**, *33*, L01304.

(53) O'Keeffe, M.; Hyde, B. G. Some Structures Topologically Related to Cubic Perovskite (E21), ReO<sub>3</sub> (D09) and Cu<sub>3</sub>Au (L12). *Acta Crystallogr., Sect. B: Struct. Crystallogr. Cryst. Chem.* **1977**, *33*, 3802–3813.

(54) O'Keeffe, M.; Hyde, B. G.; Bovin, J.-O. Contribution to the Crystal Chemistry of Orthorhombic Perovskites: MgSiO<sub>3</sub> and NaMgF<sub>3</sub>. *Phys. Chem. Miner.* **1979**, *4*, 299–305.

(55) Runge, C. E.; Kubo, A.; Kiefer, B.; Meng, Y.; Prakapenka, V. B.; Shen, G.; Cava, R. J.; Duffy, T. S. Equation of State of MgGeO<sub>3</sub> Perovskite to 65 GPa: Comparison with the Post-Perovskite Phase. *Phys. Chem. Miner.* **2006**, *33*, 699–709.

(56) Lundin, S.; Catalli, K.; Santillán, J.; Shim, S.-H.; Prakapenka, V. B.; Kunz, M.; Meng, Y. Effect of Fe on the Equation of State of Mantle Silicate Perovskite over 1 Mbar. *Phys. Earth Planet. Inter.* **2008**, *168*, 97–102.

(57) Singh, A. K. The Lattice Strains in a Specimen (Cubic System) Compressed Nonhydrostatically in an Opposed Anvil Device. *J. Appl. Phys.* **1993**, *73*, 4278–4286.

(58) Singh, A. K.; Balasingh, C.; Mao, H.; Hemley, R. J.; Shu, J. Analysis of Lattice Strains Measured under Nonhydrostatic Pressure. *J. Appl. Phys.* **1998**, *83*, 7567–7575.

(59) Akahama, Y.; Kawamura, H. Pressure Calibration of Diamond Anvil Raman Gauge to 310 GPa. *J. Appl. Phys.* **2006**, *100*, 043516.